# Retrieval of Precipitation Profiles from Multiresolution, Multifrequency Active and Passive Microwave Observations

MIRCEA GRECU

*Goddard Earth Sciences and Technology Center, University of Maryland, Baltimore County, Baltimore, and NASA Goddard Space Flight Center, Greenbelt, Maryland*

WILLIAM S. OLSON

*Joint Center for Earth Systems Technology, University of Maryland, Baltimore County, Baltimore, and NASA Goddard Space Flight Center, Greenbelt, Maryland*

EMMANOUIL N. ANAGNOSTOU

*Department of Civil and Environmental Engineering, University of Connecticut, Storrs, Connecticut*

(Manuscript received 9 June 2003, in final form 11 November 2003)

ABSTRACT

In this study, a technique for estimating vertical profiles of precipitation from multifrequency, multiresolution active and passive microwave observations is investigated. The technique is applicable to the Tropical Rainfall Measuring Mission (TRMM) observations, and it is based on models that simulate high-resolution brightness temperatures as functions of observed reflectivity profiles and a parameter related to the raindrop size distribution. The modeled high-resolution brightness temperatures are used to determine normalized brightness temperature polarizations at the microwave radiometer resolution. An optimal estimation procedure is employed to minimize the differences between the simulated and observed normalized polarizations by adjusting the drop size distribution parameter. The impact of other unknowns that are not independent variables in the optimal estimation, but affect the retrievals, is minimized through statistical parameterizations derived from cloud model simulations. The retrieval technique is investigated using TRMM observations collected during the Kwajalein Experiment (KWAJEX). These observations cover an area extending from 5° to 12°N latitude and from 166° to 172°E longitude from July to September 1999 and are coincident with various ground-based observations, facilitating a detailed analysis of the retrieved precipitation. Using the method developed in this study, precipitation estimates consistent with both the passive and active TRMM observations are obtained. Various parameters characterizing these estimates, that is, the rain rate, precipitation water content, drop size distribution intercept, and the mass-weighted mean drop diameter, are in good qualitative agreement with independent experimental and theoretical estimates. Combined rain estimates are, in general, higher than the official TRMM precipitation radar (PR)-only estimates for the area and the period considered in the study. Ground-based precipitation estimates, derived from an analysis of rain gauge and ground radar data, are in better agreement with the combined estimates than with the TRMM PR-only estimates, which suggests that information useful for improving the radar-only estimates is contained in the brightness temperature data.

## 1. Introduction

Past studies demonstrate various ways in which passive microwave information can contribute to the improvement of airborne and satelliteborne radar precipitation estimates. A straightforward option for including radiometer information in algorithms for precipitation estimation from airborne and spaceborne radar observations, such as those provided by the Tropical Rainfall Measuring Mission (TRMM) precipitation radar (PR), is to estimate the path-integrated attenuation (PIA) at the radar's frequency from radiometer observations. Because the PIA affects the radar precipitation estimates in two ways, through the reflectivity profile corrected for attenuation and through the reflectivity–precipitation relationships that are updated as a function of PIA, the accuracy of the PIA estimate is crucial. Estimates of PIA based exclusively on the reflectivity profiles are quite uncertain because of variations in the drop size distributions (DSDs), and independent considerations need to be taken into account to reduce the PIA uncertainty to acceptable levels. Meneghini et al. (2000) used a surface reference technique (SRT) to estimate the PIA,

*Corresponding author address:* Dr. Mircea Grecu, GEST/UMBC, NASA Goddard Space Flight Center, Code 912.0, Greenbelt, MD 20770.
E-mail: grecu@agnes.gsfc.nasa.gov

while Smith et al. (1997), inspired by the work of Weinman et al. (1990), derived formulas to estimate the PIA from 10-GHz radiometer observations. The benefit of using radiometer-based estimates of PIA in radar profiling algorithms has not been fully investigated, but at least theoretically the radar–radiometer estimates may lead to better results than the SRT estimates alone. Another way of including passive observations in radar rain profiling algorithms is by iteratively modifying the radar retrievals as a function of a small number of parameters (able to provide a large number of possible solutions given a profile of attenuated reflectivity) until the differences between the calculated and observed brightness temperatures are minimized. This kind of approach was explored by Grecu and Anagnostou (2002). Similar, but not fully equivalent, approaches were investigated by Schols and Weinman (1994), Olson et al. (1996), Haddad et al. (1997), Meneghini et al. (1997), Marzano et al. (1999), and Skofronick-Jackson et al. (2003).

One common characteristic of most of these approaches is that they were developed and investigated based on airborne data, assuming similar resolutions and spatial coincidence for all observations. Although some of the methods can be readily extended to satellite-based observations, which are characterized by significantly different resolutions, only a few algorithms have been formulated and implemented to retrieve precipitation from combined active and passive satellite observations. Among those, the most notable is the TRMM-combined algorithm (Haddad et al. 1997). One possible limitation of the TRMM-combined algorithm resides in the fact that the brightness temperatures associated with a given reflectivity profile are not explicitly calculated using physical models, but are estimated based on an a priori statistical relationships. Consequently, the errors in the estimated brightness temperatures may be larger than those derived from a physical model. Because the information from brightness temperatures is ''weighted'' in the retrieval as a function of the brightness temperature estimation accuracy, it follows that more accurate estimates of brightness temperatures make better use of the radiometer information. In this study, we formulate and investigate a combined technique that includes a physical, scene-dependent model for brightness temperature prediction, and provides estimates physically consistent with both radiometer and radar observations.

The technique, which is an extension of that developed by Grecu and Anagnostou (2002), is applied to retrieve precipitation profiles from TRMM Microwave Imager (TMI) and PR observations. Observations within an area extending from 5° to 12°N latitude and from 166° to 172°E longitude, made during the period July–September 1999, are considered because of their coincidence with observations from various instruments deployed in the Kwajalein Experiment (KWAJEX). A detailed description of the technique is given in the next section. The retrievals are analyzed based on indirect criteria, such as the agreement between simulated and observed brightness temperatures, the agreement between various parameters of the retrieved DSD and the disdrometer-observed DSD, and direct comparisons with ground radar rain estimates.

The paper is organized as follows: the next section describes the mathematical formulation of the combined technique; section 3 contains results from the application of the technique to the KWAJEX data; in section 4, a comparison between estimates from the combined technique and ground radar estimates is presented; conclusions and recommendations for future work are provided in section 5.

## 2. Formulation of the combined retrieval technique

The retrieval technique is an extension of the one formulated by Grecu and Anagnostou (2002). The basic radar and radiometer modeling components are essentially the same, the major difference being an adaptation of these basic components to be consistent with the characteristics of the TRMM sensors. In the earlier work, each precipitation profile could be retrieved independently of other precipitation profiles. In the current formulation, given the overlapping of passive sensor footprints, a simultaneous retrieval of a large number of profiles (encompassing large areas of precipitation) must be considered.

As remarked by Grecu and Anagnostou (2002), although the most rigorous formulation requires the quantification and inclusion of all radar observational and modeling uncertainties, a simplified formulation is preferable because it makes the solution computationally more tractable. Therefore, we consider for each precipitation profile only one parameter that influences the radar retrieved profiles or the brightness temperature simulations. This parameter is the intercept of the DSD, $N_0^*$, in a normalized gamma distribution (Testud et al. 2001):

$$N(D) = N_0^* f(\mu)\left(\frac{D}{D_0}\right)^{\mu} \exp\left[-(3.67 + \mu)\frac{D}{D_0}\right], \quad (1)$$

where

$$f(\mu) = \frac{6}{(3.67)^4}\frac{(3.67 + \mu)^{(4+\mu)}}{\Gamma(3.67 + \mu)}. \quad (2)$$

Both theoretical and observational evidence (Testud et al. 2001) indicate that most precipitation-related relationships (e.g., radar reflectivity vs rain rate, radar reflectivity vs attenuation, absorption vs precipitation content) strongly depend on $N_0^*$ and only weakly on $\mu$. Moreover, the $N_0^*$ dependence can be readily incorporated into power-law relationships, which generalize to $Y = aN_0^{*(1-b)}X^b$. For example, the Marshall–Palmer relationship, $Z = 200R^{1.6}$, which holds for $N_0^* = 0.08$ cm$^{-4}$, can be extrapolated to $Z = 200(N_0^*/0.08)^{-0.6}R^{1.6}$

and then applied for $N_0^* \neq 0.08\ \text{cm}^{-4}$. This property has been exploited in many radar profiling algorithms (Ferreira et al. 2001), including the official TRMM PR algorithm (Iguchi et al. 2000), although in the PR algorithm the multiplicative factors in the power-law relationships are not calculated explicitly as $aN_0^{*(1-b)}$, but are retrieved from a priori relationships. Thus, $N_0^*$ is determined from the condition that the PIA determined from the reflectivity profile is equal to the independent estimate of the PIA (from SRT or radiometer-based estimates; Weinman et al. 1990; Smith et al. 1997). In our formulation, the PIA is neither directly estimated from passive observations nor is it equated to the radar algorithm–produced PIA in order to determine $N_0^*$. Instead, $N_0^*$ is determined iteratively by minimizing the differences between observed and model-simulated microwave brightness temperatures. This will become more evident in the discussion that follows.

There are obviously other variables that influence the radar retrievals and the radiative transfer calculations, but their effect is somewhat smaller and they are not considered free variables in the retrievals. Instead, these variables are parameterized as functions of other variables. For example, the nonprecipitating cloud water profile is described by a generic profile with a magnitude that is determined as a function of the reflectivity profile, using a regression derived from cloud model simulations. This is similar to the formulation of Hinton et al. (1992). The precipitation transition from snow and graupel to rain is described using models similar to those used in the TRMM PR facility algorithm (Iguchi et al. 2000). That is, for stratiform profiles with a detectable bright band, the precipitation is assumed to consist exclusively of rain (snow–water mixture with less than 1.7% water) 500 m below (above) the bright band. In the 1000-m-deep layer, including the bright band, the same model as that of Iguchi et al. (2000) is used. For stratiform profiles without a bright band and for convective profiles, a similar model is used, but with a 1.5-km-deep transition layer centered on the freezing level. The snow density is modeled using the Magono and Nakamura (1965) formula (see Grecu and Anagnostou 2002), and the snow particle size distribution is derived from the size distribution of the drops resulted from the melting snow. The melted particles are assumed to follow a normalized gamma distribution. The simulated brightness temperatures depend on the choice of a phase transition model, but for low frequencies (10 and 19 GHz) the dependency is not strong, which makes the use of the aforementioned models acceptable. A composite sounding, constructed from the sounding data collected during KWAJEX, is used to describe the vertical distribution of temperature and humidity. If a bright band is present, the temperature profile is modified by an offset that makes the temperature at the height of the bright band approximately 3.5°C, as suggested by various melting-layer models (Olson et al. 2001).

Each reflectivity profile is associated with a DSD intercept $N_0^*$ in the retrieval. Given the DSD parameter, that is, $N_0^*$, and the reflectivity profiles, we simulate brightness temperatures at the radar resolution. Then we convolve the brightness temperatures at the resolution of the TRMM sensors, and, based on the differences between simulations and observations, we update the $N_0^*$ values. The radar retrieval algorithm and the radiative transfer model are fully described in Grecu and Anagnostou (2002). A Bayesian maximum likelihood formulation, similar to that of Grecu and Anagnostou (2002), but extended to account for the spaceborne sensor resolution, is derived in terms of a functional that provides optimal estimates through its minimization. In this functional, normalized polarization differences are used instead of brightness temperatures. From Petty (1994), the normalized polarization (NP) is defined as

$$\text{NP} = \frac{T_V - T_H}{T_{V,\text{clear}} - T_{H,\text{clear}}}, \tag{3}$$

where $T_V$ and $T_H$ are the vertically and horizontally polarized brightness temperatures and $T_{V,\text{clear}}$ and $T_{H,\text{clear}}$ are background brightness temperatures interpolated from brightness temperatures in adjacent rain-free areas. The use of the normalized polarization minimizes the impact of some unknowns, such as the surface emissivity, water vapor concentration, and so on, that are not considered free parameters in the estimation method. As an example, a precipitation field and the associated 19-GHz emission index, here defined as $1 - \text{NP}$, is represented in Fig. 1. The emission index is better suited for graphical representations than the normalized polarization because it is 0 for 0 rain rate and increases with the rain rate. It may be noted from Fig. 1 that the emission index is strongly correlated with the rain rate.

The combined retrieval from passive and active observations requires the minimization of the following functional:

$$\begin{aligned} F = {} & \frac{1}{2}\left[\mathbf{NP}^M - \int_E \mathbf{G}(A)\mathbf{NP}_A(A, \tilde{\mathbf{X}}_Q, \tilde{\mathbf{N}}_0^*)\, dA\right]^{\mathrm{T}} \\ & \times \mathbf{W}_T^{-1}\left[\mathbf{NP}^M - \int_E \mathbf{G}(A)\mathbf{NP}_A(A, \tilde{\mathbf{X}}_Q, \tilde{\mathbf{N}}_0^*)\, dA\right] \\ & + \frac{1}{2}(\mathbf{M}_N - \tilde{\mathbf{N}}_0^*)^{\mathrm{T}}\mathbf{W}_N^{-1}(\mathbf{M}_N - \tilde{\mathbf{N}}_0^*) \\ & + \frac{1}{2}[\mathbf{PIA}_S - \mathbf{PIA}(\tilde{\mathbf{X}}_Q, \tilde{\mathbf{N}}_0^*)]^{\mathrm{T}} \\ & \times \mathbf{W}_{\text{PIA}}^{-1}[\mathbf{PIA}_S - \mathbf{PIA}(\tilde{\mathbf{X}}_Q, \tilde{\mathbf{N}}_0^*)]. \end{aligned} \tag{4}$$

In (4), $\mathbf{NP}^M$ is a three-dimensional array of observed normalized polarizations, that is, a two-dimensional array for each frequency, $E$ is the region viewed by the instruments, $\mathbf{G}$ is the antenna gain function, $\mathbf{NP}_A$ is an array of normalized polarizations calculated from radar retrievals, $\tilde{\mathbf{X}}_Q$ is an array of radar-retrieved hydrometeor contents, $\tilde{\mathbf{N}}_0^*$ is an array of $N_0^*$ values, $\mathbf{M}_N$ is the mean

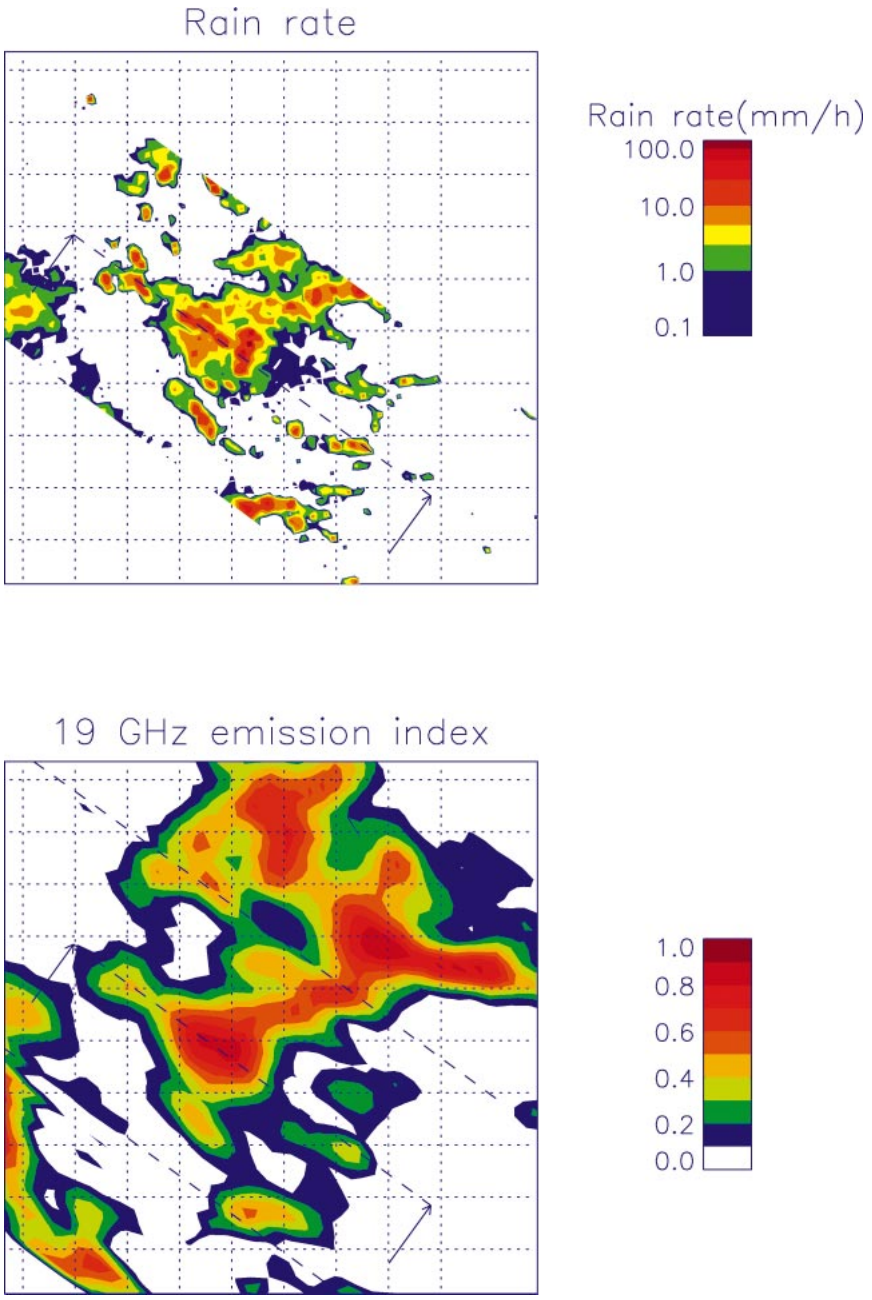


FIG. 1. (top) Surface rain rate and (bottom) 19-GHz emission index for TRMM orbit 9540 over Kwajalein Island. The inner dashed line in the bottom panel indicates the cross section in Fig. 3; the outer dashed lines represent the boundaries of the PR swath.

of $\tilde{\mathbf{N}}_0^*$, and $\mathbf{W}_N$ is an a priori estimate of the $N_0^*$ spatial covariance. The second term on the right-hand side of (4) makes the problem better posed by imposing some conditions on the spatial variability of $N_0^*$. The variable $A$ under the integral is a dummy variable indicating an elemental area in the sampling area $E$. In the present application, $dA$ is the PR's footprint. In the third term on the right-hand side, **PIA** is the model predicted array of PIA, while $\mathbf{PIA}_s$ is a surface return–based estimate of PIA. All variables denoted **W** are covariance matrices indicating the confidence in observations and simulations. Note that the exponential of function $F$ is the (unnormalized) probability function of $\tilde{\mathbf{N}}_0^*$ given $\tilde{\mathbf{X}}_Q$, $\mathbf{PIA}_s$, and $\mathbf{NP}^M$, and assuming that the differences between the actual values of these variables and their a priori models are Gaussian. A derivation for a slightly different formulation may be found in Marzano et al. (1999).

The minimization of (4) is achieved as follows. Given a set of $N_0^*$s (a value for each reflectivity profile), a retrieval is performed for each profile using exclusively the PR observations. The radar profiling algorithm is presented in Grecu and Anagnostou (2002). From the radar retrievals, denoted by $\tilde{\mathbf{X}}_Q$ in (4), the NPs are calculated using a modified Eddington model (Bauer et al. 1998), and all of the terms of $F$ are evaluated. The gradient of $F$ with respect to the $N_0^*$s is also evaluated, and a gradient-based optimization procedure is used to minimize (4). An efficient methodology for calculating the gradient of $F$, namely, the reverse evaluation (Giering and Taminski 1998), is employed in this study. The reverse, or adjoint, evaluation, exploits the fact that $F$ is a scalar consisting of a linear combination of various variables. One may interpret the procedures that evaluate $F$ as a sequence of numerical transforms that map input variables into output variables. For the gradient evaluation, the Jacobian matrices, that is, the derivatives of the output variables with respect to the input variables, of these transforms need to be computed. The direct evaluation of $F$'s gradient requires the multiplication of the Jacobian matrices, followed by the multiplication of the final Jacobian product with a vector (the vector that combines the various squared errors into a scalar). The reverse evaluation starts by multiplying the last Jacobian matrix with the vector that combines the squared errors. The result, which is a vector, is multiplied with the Jacobian before the last and so on. In this way, the matrix times matrix operations specific to the direct evaluation are replaced by matrix times vector operations in the reverse evaluation. Consequently, the evaluation of the gradient in the reverse mode becomes similar in terms of computational time to the evaluation of the function $F$ itself (Giering and Taminski 1998). Although computationally more intensive than radar-only or TMI-only retrievals, an efficient implementation employing precomputed elements, such as emissivities, Mie factors, etc., is not prohibitively time-consuming and can be employed on most current computer systems.

The choice of $\mathbf{W}_{\text{PIA}}$ is made using the methodology in Grecu and Anagnostou (2002); $\mathbf{W}_T$ is determined based on an analysis involving cloud resolving model (CRM) simulations. The Goddard Cumulus Ensemble (GCE) model is used in this analysis. GCE features a bulk parameterization, with five species of hydrometers (cloud water, cloud ice, rain, snow, and graupel) described by exponential distributions with constant intercepts (Tao and Simpson 1993). GCE-simulated fields of atmospheric variables (i.e., hydrometeor contents, humidity, temperatures, etc.) are considered the truth in the analysis and are used to derive fields of brightness temperatures and attenuated reflectivity profiles at TRMM instrument frequencies and resolutions. The same drop size distributions assumed in the GCE parameterization are used for brightness temperature and reflectivity calculations. From the synthetic reflectivity profiles, hydrometeor fields are derived based on the simplified model of vertical hydrometeor structure presented above. In these synthetic retrievals, $N_0^*$s are assumed known and set to the values of intercepts considered in the GCE parameterizations. The reason for assuming that $N_0^*$ is known resides in the necessity of distinctly quantifying the impact of the vertical hydrometeor structure model on radiative transfer calculations. This is because even if the $N_0^*$ values were known exactly, the PR-only retrievals would be subject to errors due to uncertainties concerning the hydrometeor type and physical properties (densities, refractive indices, etc.). These errors further propagate in radiative transfer calculations due to additional uncertainties in various variables, such as the cloud water, cloud ice, and water vapor contents—variables that cannot be exactly determined but only statistically estimated. To assess these errors, the synthetic PR-only retrieved hydrometeor fields are augmented with cloud water, water vapor, and humidity fields, as previously mentioned, and brightness temperatures at the TRMM instrument frequencies and resolutions are calculated. From these brightness temperatures NPs are derived, and those corresponding to the brightness temperatures synthesized from the true atmospheric variables (as provided by GCE and not involving any retrieval or approximate representation) are also derived. The differences between the NPs derived from retrievals and the true NPs are an approximation of the NP errors, and $\mathbf{W}_T$ is set to their covariance. Based on these calculations, the 85-GHz NP is deemed unreliable and is not considered in the retrieval. Therefore, only the 10-, 19-, and 37-GHz NPs are used.

The uncertainty in $N_0^*$ values determined from the minimization of (4) may be evaluated using the formula

$$\mathbf{W}_{N_0^*}^{-1} = \left[\frac{\partial \int_E \mathbf{G}(A)\mathbf{NP}_A(A, \tilde{\mathbf{X}}_Q, \tilde{\mathbf{N}}_0^*)\, dA}{\partial \tilde{\mathbf{N}}_0^*}\right] \times \mathbf{W}_T^{-1}\left[\frac{\partial \int_E \mathbf{G}(A)\mathbf{NP}_A(A, \tilde{\mathbf{X}}_Q, \tilde{\mathbf{N}}_0^*)\, dA}{\partial \tilde{\mathbf{N}}_0^*}\right]^{\mathrm{T}} + \mathbf{W}_N^{-1} + \left[\frac{\partial \mathbf{PIA}(\tilde{\mathbf{X}}_Q, \tilde{\mathbf{N}}_0^*)}{\partial \tilde{\mathbf{N}}_0^*}\right]\mathbf{W}_{\text{PIA}}^{-1}\left[\frac{\partial \mathbf{PIA}(\tilde{\mathbf{X}}_Q, \tilde{\mathbf{N}}_0^*)}{\partial \tilde{\mathbf{N}}_0^*}\right]^{\mathrm{T}}, \quad (5)$$

where $\mathbf{W}_{N_0^*}$ is the covariance matrix of the errors associated with $N_0^*$. Denoting by $f$ the model used to estimate the precipitation from radar observations given a set of $N_0^*$, that is $\tilde{\mathbf{X}}_Q = f(\mathbf{Z}, \tilde{\mathbf{N}}_0^*)$, where $\mathbf{Z}$ are the observed reflectivities, the uncertainty in $\tilde{\mathbf{X}}_Q$ may be estimated as

$$\mathbf{W}_{X_Q} = \frac{\partial f(\mathbf{Z}, \tilde{\mathbf{N}}_0^*)}{\partial \tilde{\mathbf{N}}_0^*}\mathbf{W}_{N_0^*}\frac{\partial f(\mathbf{Z}, \tilde{\mathbf{N}}_0^*)^{\mathrm{T}}}{\partial \tilde{\mathbf{N}}_0^*} + \mathbf{W}_f, \quad (6)$$

where $\mathbf{W}_f$ is the uncertainty associated with model $f$

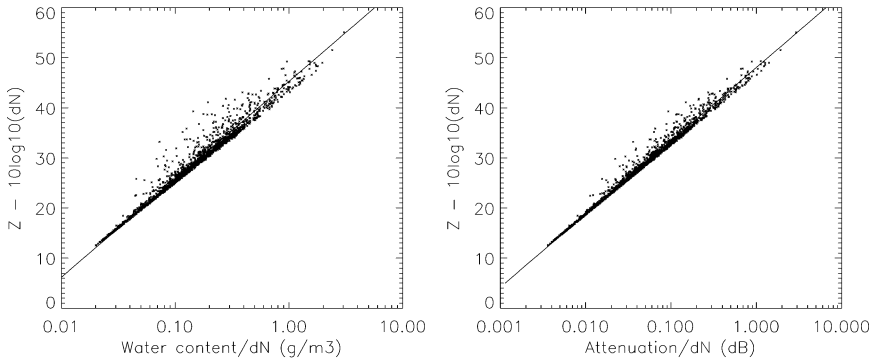


FIG. 2. Normalized reflectivity plotted against normalized specific water content, and normalized reflectivity plotted against normalized attenuation at the PR footprint resolution.

and is estimated using a methodology similar to that employed to estimate $\mathbf{W}_T$. That is, the synthetic PR retrievals are compared with the true values and their differences are considered as errors in $f$, and $\mathbf{W}_f$ is set to their covariance. It should be mentioned that the magnitude of $\mathbf{W}_f$ is more likely larger than this estimate, but more complete information regarding the transition of hydrometeors from one phase to another and their electromagnetic properties, as well as the vertical and horizontal distribution of $N_0^*$, is necessary for a better quantification.

The estimation of $\mathbf{W}_N$ and the reflectivity–precipitation and reflectivity–attenuation relationships are determined using polarimetric radar observations. As noted in previous studies, the variability of precipitation within the radar sampling volume may result in errors in precipitation estimates (Kozu and Iguchi 1999). To derive relationships that account for this variability, the following analysis was performed. Estimates of $N_0^*$ and the precipitation content are derived using polarimetric radar observations from the Texas and Florida Underflights (TEFLUN-B) experiment. The relationships derived by Bringi et al. (2003) to estimate $N_0^*$ from reflectivity, differential reflectivity, and specific differential phase are used. The estimates are aggregated up to the TRMM PR resolution. If one denotes by $dN$ the ratio of the actual $N_0^*$ to a reference $N_0^*$, say 0.08 cm$^{-4}$, then the ratio of specific water content $q$ to $dN$, or $q/dN$, and the ratio of reflectivity to $dN$, or $Z/dN$, should be linearly related in a log–log representation, if the DSD obeys a normalized gamma distribution law (Testud et al. 2001). However, when the DSDs are averaged to the PR resolution, changes are expected in the behavior of the $q/dN$–$Z/dN$ relationships. A plot of $Z/dN$ versus $q/dN$ on a logarithmic scale is given in Fig. 2. One may notice a departure from linearity that is due to precipitation variability within the PR footprints. However, the number of points that depart from straight line behavior is relatively small (about 5%), and a power law still seems adequate. The same is true for the attenuation versus reflectivity relationship. Consequently, power-law relationships used in the radar profiling algorithm are derived based on the data in Fig. 2. These relationships may be deficient for lighter rain rates, characterized by small reflectivity (e.g., smaller than 35 dB$Z$) when both the DSD model and the polarimetric radar estimates may be erroneous, but, unfortunately, no basis for deriving better relationships exists. In an area as large as a 10-GHz TMI footprint, $\mathbf{W}_N$ is calculated as the covariance of $N_0^*$. The analysis of a scaling parameter $H$ that relates the large-scale features to the small-scale variability of precipitation (Perica and Foufoula-Georgiou 1996) indicates a distribution that does not appear to be location dependent. Specifically, the scaling parameter determined from the TEFLUN-B and KWAJEX storms exhibits similar distributions, which suggests that the $N_0^*$-dependent reflectivity–precipitation relationships derived from TEFLUN-B data can be applied anywhere in the Tropics.

In the next section, the formulation described here is applied to 3 months of TRMM data and the results are analyzed.

## 3. Application to the KWAJEX data

The combined algorithm described in the previous section, or normalized polarization combined algorithm (NPCA), due to the use of normalized polarizations, is applied to 3 months of TRMM data, from July to September 1999, in a region extending from 5° to 12°N latitude and 166° to 172°E longitude. There are 83 TRMM orbits with significant rain (more than 10% raining pixels) in this dataset. The advantage of analyzing this dataset over other possible datasets is the availability of data from additional instruments, such as radars, wind profilers, disdrometers, rain gauges, and so on that were utilized during KWAJEX. KWAJEX observations were centered on the permanent ground validation site on the Kwajalein Atoll of the Republic of the Marshall Islands during the period from 23 July to 15 September 1999. KWAJEX was designed to address scientific issues related to the generation of TRMM satellite products over the tropical open ocean. Although the set of coincident TRMM and ground observations

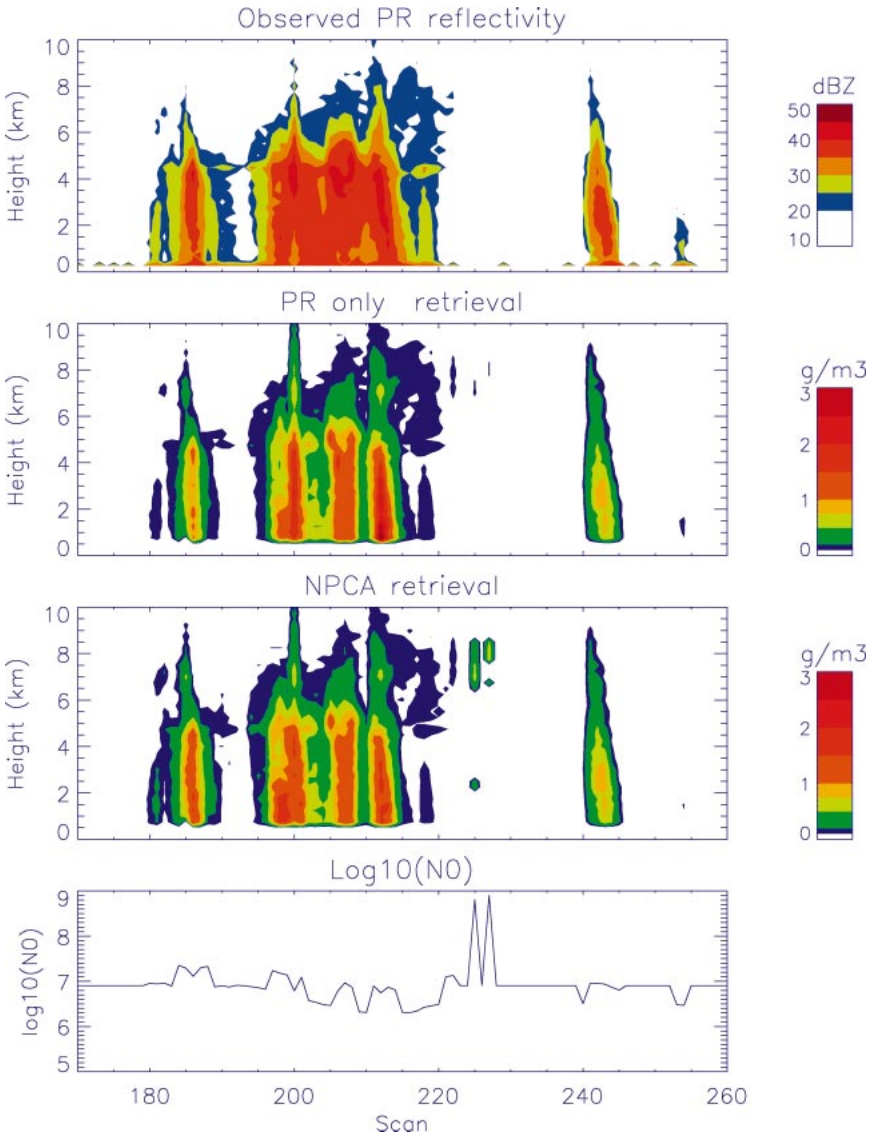


FIG. 3. The observed PR reflectivities, retrieved precipitation water contents, and retrieved normalized gamma distribution intercept $N_0^*$.

is quite limited, the set of independent observations is large, which allows for statistically significant analyses of retrievals.

In Fig. 3, an example of retrievals from the NPCA and a PR-only algorithm is presented. The PR-only algorithm is a special case of the formulation described in section 2. Specifically, the first term in (4) is not considered, and only information from the SRT and spatial variation of $N_0^*$ is used in the retrieval. A plot of the retrieved values of $\log_{10}(N_0^*)$ is also given. An inspection of Fig. 3 reveals differences between the two types of retrievals. For some profiles, the NPCA indicates larger values of specific water content than those obtained from the PR-only algorithm, while for other profiles the opposite is true. This is an indication that there is additional information in the brightness temperature observations, and its use may lead to different results in the estimation problem. Aside from two unrealistic values of $N_0^*$ and their associated profiles, the retrieved variables appear to be reasonable and consistent with what one would expect based upon cloud microphysical processes. For example, the relatively low values of $N_0^*$ between scans 200 and 220 is consistent with a greater proportion of stratiform precipitation, while the larger values between scans 180 and 190 may be representative of convective processes (coalescence and breakup). The two outliers are, most likely, a result of the PR's inability to detect precipitation with a signal weaker than 17 dBZ. That is, the extinction in volumes of precipitation that is not detected by the PR, but present in the polarization differences observed by the TMI, may be wrongly attributed to nearby precipitation de-

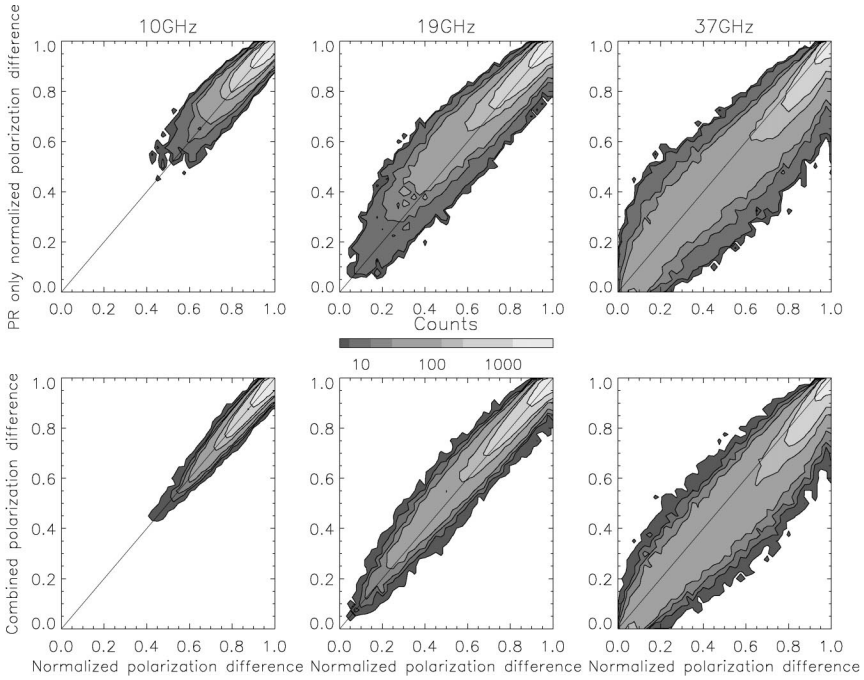


FIG. 4. Frequency plots of calculated vs observed normalized polarization differences. (top) Polarization differences derived from a PR-only retrieval, and (bottom) polarization differences derived from the NPCA.

tected by the PR (resulting in very large $N_0^*$ values). However, anomalous retrievals, such as the two in Fig. 3, are not frequent (statistical analyses reveal an insignificant number of extreme values of $N_0^*$).

Figure 4 provides more general results, based upon the full KWAJEX dataset. The 10-, 19-, and 37-GHz NPs calculated from the PR-only retrieval and the NPCA retrieval are plotted against corresponding observed NPs. Frequency maps rather than scatterplots are used, given the large number of points considered in the analysis. One may note that the NPs at 10 and 19 GHz, calculated in the absence of radiometer information, are in general higher than the observed values. This implies, at least in the realm of our physical models, that the extinction in the atmospheric columns sampled by the TMI is generally underestimated by the PR-only algorithm, and, therefore, precipitation amounts are underestimated. When the radiometer information is used in the retrieval, significantly better agreement between the calculated and observed NPs is achieved. The best agreement is obtained at 10 GHz, and the agreement deteriorates with increasing frequency. This might be explained by two factors. First, the resolution of the TMI channels increases with frequency, leading to larger random errors in calculated NPs at higher frequencies. This is because the calculation of NP for the low-frequency channels involves more smoothing by convolution and a greater reduction of random errors. Second, the low-frequency channels are less sensitive to errors caused by variables that cannot be directly observed, such as cloud water, the density of frozen and mixed hydrometeors, and so on. Nevertheless, better agreement between calculated and observed NPs is obtained at all frequencies (although there is only marginal improvement at 37 GHz), implying that better-defined solutions are obtained with the inclusion of the passive information. While the 19-GHz NPs determined from the NPCA retrievals are slightly higher than the observed values, the 37-GHz NPs are slightly lower, with more noticeable differences at 37 GHz. This is most likely an effect of uncertainties, such as the variability of cloud water content, and the variability in the density–diameter relationships for frozen hydrometeors, that do not have a large impact on the calculation of brightness temperatures at a low frequency. The fact that the NPCA solution exhibits a better agreement in terms of NPs at lower frequencies indicates that the algorithm deals appropriately with uncertainties and gives more weight to less uncertain models.

In Fig. 5, the distribution of retrieved surface liquid water contents and DSD intercepts ($N_0^*$) for PR-only and NPCA retrievals are shown. In this study, the estimates are classified as convective or stratiform using the TRMM PR facility algorithm's classification (product 2A23). It is apparent from Fig. 5 that, in absence of radiometer information, there are no significant changes in $N_0^*$ for stratiform cases. This is an indication that the SRT estimates are not used at small PIAs. For convective cases, the SRT impacts the PR-only retrieval, and distinct $N_0^*$ values are obtained in the retrieval.

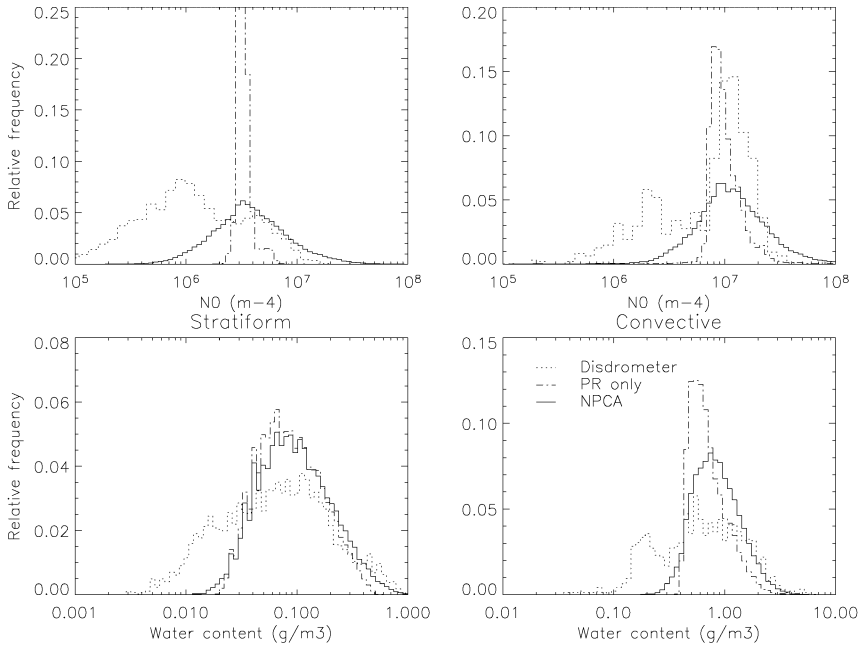


FIG. 5. Frequency plots of the precipitation water contents and normalized gamma distribution intercept $N_0^*$ from PR-only and NPCA retrievals, as well as observations.

When the TMI information is considered in the retrieval, a broader distribution of $N_0^*$ values is obtained. Although not obvious from the distribution of water contents, especially for stratiform precipitation, the water contents in the NPCA retrievals are about 12% larger than those from the PR-only retrievals. This is consistent with the results in Fig. 4, which suggest an underestimation of precipitation by the PR-only algorithm. The uncertainties in the hydrometeor estimates expressed in terms of error standard deviation are, according to the estimates from (5) and (6), usually less than 30% of the retrieved values given by (4).

Distributions of water content and $N_0^*$ from disdrometer data are included in Fig. 5 for reference. Joss–Waldvogel disdrometer data from 14 July 1999 to 29 August 1999 are used to build the histograms shown. It may be noted that there are some differences between the distributions of water content and $N_0^*$ from satellite and disdrometer observations. The satellite observations seem deficient in estimating small-value water contents. This may be due to the precipitation variability within the PR footprint and/or the limited PR sensitivity. Both of these issues are difficult to investigate, even with polarimetric radar observations, because of the reliability of the observations, and, consequently, because of the precipitation estimates that are derived from them, which decrease with decreasing reflectivity. Various parameters such as the specific differential phase and differential reflectivity are usually noisy in regions characterized by low reflectivity or rain intermittency, which precludes the reliable estimation of DSDs in such regions. However, despite the differences between the disdrometer and satellite distributions of water contents and $N_0^*$, the parameterizations used in the NPCA retrievals and the associated values of retrieved variables are deemed appropriate. Results that support this conclusion will be presented in the next section.

One DSD parameter that is usually analyzed in conjunction with $N_0^*$ is the mean mass-weighted diameter $d_m$. This parameter is defined as the ratio of the fourth moment of the DSD to the third moment of the DSD. The analysis of ($N_0^*$, $d_m$) couples does not reveal any strong relationship between the two parameters (Fig. 6). This result is consistent with the findings of Bringi et al. (2003), who did not find strong relationships between $N_0^*$ and $d_m$, but noted a trend; that is, large values of $N_0^*$ are associated with small values of $d_m$ and vice versa. The decrease of $N_0^*$ with increasing $d_m$ may be explained by the aggregation of snow to form stratiform rain and the evaporation of that rain in weakly subsiding air. Both theoretical and experimental studies (Passarelli and Srivastava 1979; Stewart et al. 1984) indicate that snow aggregation leads to fewer, larger snow particles. Below the freezing level, the hydrometeors undergo complex processes consisting of melting, evaporation, coalescence, and breakup (Stewart et al. 1984). Hu and Srivastava (1995) found that these process lead to DSDs that reach an equilibrium state and depend on the snow particle size distribution above the freezing level. Therefore, the $d_m$–$N_0^*$ dependence in snow particle size distributions translates to a $d_m$–$N_0^*$ dependency in rain DSDs. In addition to this, evaporation reduces the number of small drops and increases the percentage of large drops (Li and Srivastava 2001), thereby increasing $d_m$.

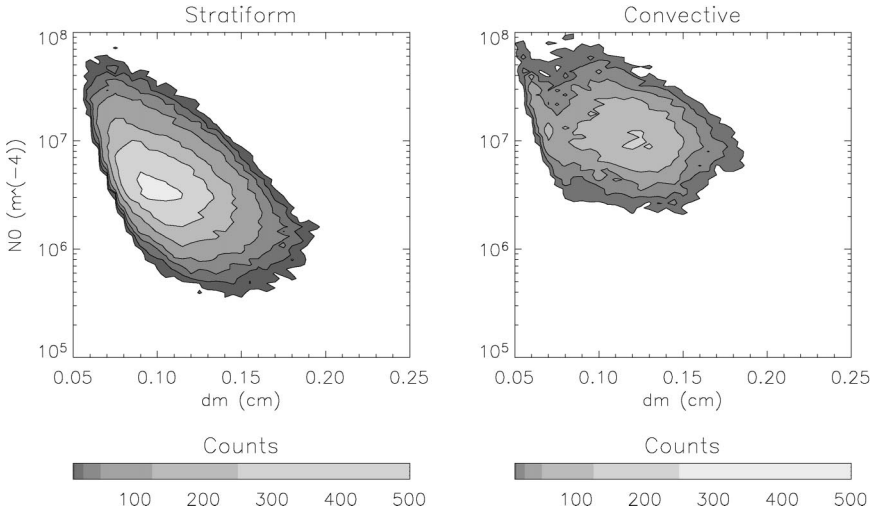


FIG. 6. Frequency plots of the normalized gamma distribution intercept $N_0^*$ plotted against the mass weighted mean diameter $d_m$.

For convective rain, coalescence, breakup, and evaporation are responsible for the $d_m$–$N_0^*$ dependency. Numerical calculations (Hu and Srivastava 1995) show that convective DSDs tend to attain an equilibrium state in two phases. In the first phase, the DSDs rapidly reach a state in which the collisional processes (coalescence and breakup) counteract each other. In the second phase, the DSDs are further shaped by evaporation. The efficiency of collisional processes depends on various factors (Khain et al. 2000), such as the air vertical velocity, turbulence, and the nonuniformity of cloud droplet concentration, and more efficient processes lead to a DSD broadening and $N_0^*$ reduction. This explains the existence of a multitude of equilibrium DSDs. In the present study, the convective and stratiform regions are overlapping in the ($N_0^*$, $d_m$) plane, unlike the findings of Testud et al. (2001), who observed a more distinct separation. This is probably a consequence of the fact that $N_0^*$ and $d_m$ are not explicitly determined from drop counts, but from various integrated variables such as reflectivity, PIA, brightness temperatures, etc. It may be also be a consequence of the way the convective stratiform classification is done in this study.

The rain rates estimated by the NPCA are strongly correlated with those from the TRMM PR facility algorithm (version-5 2A25 rain product; see Fig. 7). The strong correlation between the 2A25 estimates and the NPCA estimates is a consequence of the fact that the algorithms are based on the same general formalism. However, the average rain rate from the NPCA algorithm is about 30% greater than the average 2A25 rain rate. About 7%–8% of this difference may be explained by the different parameterization of the $Z$–$R$ relationship used by the NPCA. In other words, even if the $N_0^*$

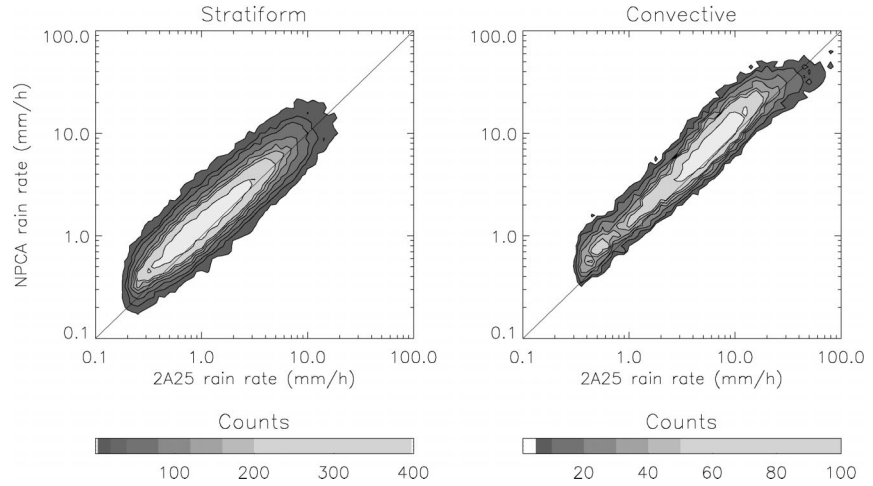


FIG. 7. Frequency plots of 2A25 rain rates vs NPCA rain rates for convective and stratiform regions.

TABLE 1. Sensitivity of NPCA estimates with respect to covariance matrices.

| Experiment No. | 1 | 2 | 3 | 4 | 5 | 6 | 7 |
|---|---|---|---|---|---|---|---|
| $\mathbf{W}_T\mathbf{W}_T^n$ | 1.0 | 2.0 | $\infty$ | 1 | $\infty$ | 0.5 | $\infty$ |
| $\mathbf{W}_{\text{PIA}}/\mathbf{W}_{\text{PIA}}^n$ | 1.0 | 1.0 | 1.0 | 2.0 | 2.0 | 0.5 | 0.5 |
| $<w>/<w^n>$ | 1.00 | 0.97 | 0.88 | 0.94 | 0.83 | 1.02 | 0.99 |

retrieved from 2A25 (Ferreira et al. 2001) is used in the NPCA parameterization, a difference of 7%–8% between the 2A25 and NPCA rainfall-rate estimates remains. Therefore, the bulk difference (22%–23%) is exclusively the effect of the $N_0^*$ estimation based on the TMI brightness temperatures. As indicated by Fig. 4, the PR-only estimates seem low from the TMI observation standpoint, and so the inclusion of the TMI data in the NPCA leads to higher estimates.

To analyze the NPCA's sensitivity to errors in covariance matrices, retrievals with different formulations for the covariance matrices are performed. The sensitivity tests are performed because cloud model simulations, especially those employing bulk parameterizations, can provide only a partial and approximate description of the variables on which brightness temperatures and reflectivity factors depend. Therefore, the methodology described in section 2 may underestimate some errors in radiative transfer calculations, while overestimating others, and, consequently, $\mathbf{W}_T$ is subject to uncertainties. Similarly, the estimated $\mathbf{W}_{\text{PIA}}$ is based on statistical considerations, which may not reflect all of the physical mechanisms that lead to errors in SRT PIA estimates. On the other hand, the precipitation estimates that follow from the minimization of (4) depend on $\mathbf{W}_T$ and $\mathbf{W}_{\text{PIA}}$, which justify a sensitivity analysis. Consequently, a series of retrievals with $\mathbf{W}_T$ and $\mathbf{W}_{\text{PIA}}$ different from the nominal formulations described in section 2, denoted here as $\mathbf{W}_T^n$ and $\mathbf{W}_{\text{PIA}}^n$, are performed. The new covariance matrices differ from the nominal one not in structure but in magnitude. That is, $\mathbf{W}_T = x\mathbf{W}_T^n$ and $\mathbf{W}_{\text{PIA}} = y\mathbf{W}_{\text{PIA}}^n$, where $x$ and $y$ are scalars. The actual values of $x$ and $y$ are given in Table 1. There are seven experiments (retrievals) reported in Table 1. The first three experiments are characterized by constant $y$ ($y = 1$), and increasing $x$ (from 1 to infinity). Note that an infinite value for the $\mathbf{W}_T/\mathbf{W}_T^n$ ratio corresponds to a PR-only retrieval. In experiments 4 and 5, $y = 2.0$ and $x$ is variable, while in experiments 6 and 7, $y = 0.5$ and $x$ is variable. Thus, the seven experiments are devised to provide a sampling in the $(x, y)$ space conducive to conclusive results. Also presented in Table 1 are the ratios $(\langle w\rangle/\langle w^n\rangle)$ of mean water contents for each retrieval of the mean water contents retrieved based upon the nominal covariance matrices.

The results in Table 1 indicate the NPCA's dependence on the choice of the covariance matrices. The dependence is quite strong with respect to $\mathbf{W}_{\text{PIA}}^n$ and is weaker with respect to $\mathbf{W}_T^n$. It follows that PR-only retrievals are quite sensitive to the choice of $\mathbf{W}_{\text{PIA}}$, while retrievals incorporating passive information are less dependent on the actual magnitudes of the covariance matrices. The fact that the PR-only retrieval with $\mathbf{W}_{\text{PIA}} = 0.5\,\mathbf{W}_{\text{PIA}}^n$ leads to a solution magnitude-wise very similar to the nominal one is possibly fortuitous, or it may be due to an overestimation of $\mathbf{W}_{\text{PIA}}^n$. Therefore, although estimates from a PR-only retrieval may be very similar to those from a combined retrieval in terms of large space–time means, a combined retrieval is preferable because it lends more credence to the results. Moreover, as indicated by (5) and (6), the instantaneous, small-scales estimates from a combined approach have less uncertainty. In the next section, NPCA precipitation estimates are compared with estimates from ground-based radar.

## 4. Comparison with ground radar estimates

Although the estimation of precipitation from ground-based radar observations may be subject to quite large uncertainty (Anagnostou and Krajewski 1999), a comparison between ground radar and satellite estimates of precipitation is useful for characterizing the performance of satellite precipitation estimation algorithms. A similar view was expressed by Liao et al. (2001), who compared rain rates and reflectivity factors derived from the TRMM PR and the Weather Surveillance Radar-1988 Doppler (WSR-88D) at Melbourne, Florida.

The ground radar precipitation estimates used in this study are produced by the TRMM Ground Validation Office at the NASA Goddard Space Flight Center. One characteristic of these estimates is that they incorporate rain gauge information, using a multistep procedure that includes the following components. First, a quality-control procedure is applied to both radar and gauge data and false or unreliable data are discarded. While the rain gauge quality-control procedure is designed to identify malfunctioning gauges, the radar quality-control procedure is applied to remove nonmeteorological echoes, such as those due to clutter associated with insects, birds, chaff, wildfire, and anomalous propagation. Second, separate $Z$–$R$ relationships are applied to convective and stratiform rain echoes, and monthly accumulations for both convective and stratiform precipitation are calculated. Third, the monthly accumulations from gauge observations are calculated within the radar observation area, and, based on these, the multiplicative coefficients in the $Z$–$R$ relationships are adjusted to force agreement between the radar and gage accumulations. Although the radar rain-rate estimates produced by this procedure may still be subject to large uncertainty at small space and time scales, they are appropriate for large space–time scales. Kwajalein ground radar precipitation estimates were produced by the TRMM Ground Validation Office for almost the entire TRMM operation period, but only 3 months, July–September 1999, are considered in this analysis. These 3 months of data provide a statistically significant analysis without

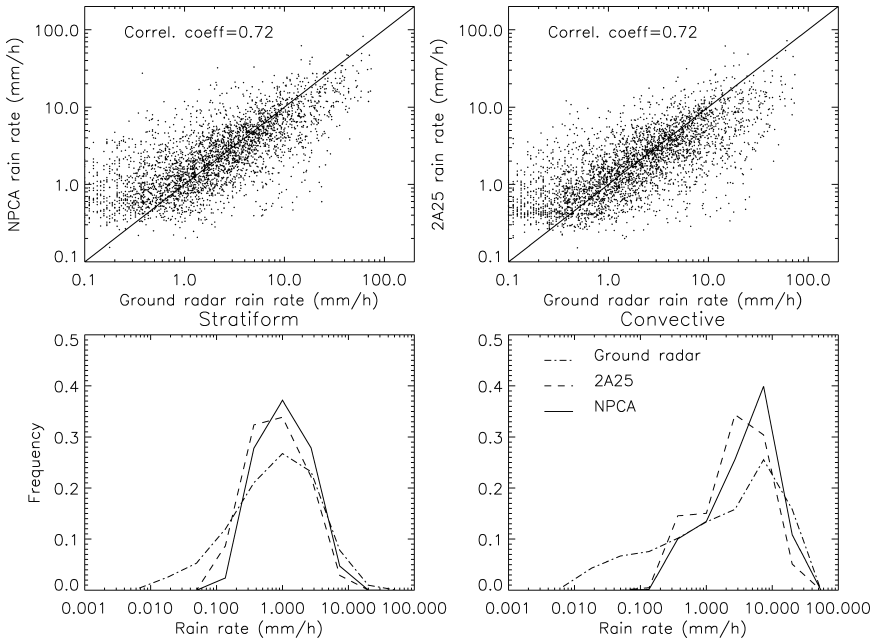


FIG. 8. TRMM and ground radar estimates. (top left) Scatterplot of NPCA rain rates vs ground radar rain rates; (top right) scatterplot of 2A25 rain rates vs ground radar rain rates; histograms of ground radar, NPCA, and 2A25 rain rates for (bottom left) stratiform and (bottom right) convective precipitation.

demanding large computer resources, that is, disk space and computational time.

The NPCA estimates and the ground radar estimates are well correlated, as are the 2A25 rain and the ground radar estimates (Fig. 8). A systematic overestimation of low-intensity rain relative to the ground radar estimates by both NPCA and version-5 2A25 is apparent from Fig. 8. This is probably a consequence of the precipitation variability within the PR sampling volume. It is worth noting that although the 2A25 and the NPCA deal differently with this variability, they perform similarly at low rain rates. Moreover, a comparison between the TRMM combined facility algorithm (2B31) yields similar results (not shown in the figure). However, the three algorithms, that is, the NPCA, 2A25, and 2B31, produce significantly different mean rain rates (Table 2), which suggests that, for long-term and large-scale applications, the choice of a particular algorithm does make a difference. The ground radar estimates are higher than the 2A25 and 2B31 estimates, and agree better with the radiometer-based NPCA estimates. The results in Table 2 support the idea that the brightness temperature data contain additional information, which, through the adjustment of DSD parameters, can be used to improve rain-rate estimates.

TABLE 2. Mean rain rates from ground radar and different TRMM algorithms. The mean is computed for coincident TRMM and Kwajalein radar observations over the period Jul–Sep 1999.

| Estimator | Ground radar | NPCA | 2A25 | 2B31 |
|---|---|---|---|---|
| Mean rain rate (mm $h^{-1}$) | 3.60 | 3.33 | 2.61 | 2.82 |

Although all estimates in this study, that is, ground-based radar, 2A25, 2B31, and NPCA estimates, are subject to uncertainties, and though an accurate quantification of these uncertainties is difficult, the evidence presented here indicates that the NPCA fits well in the general TRMM rainfall estimation effort. Kummerow et al. (2001) found a positive bias varying from 20% to 40% in version-5 rain estimates from the TRMM TMI facility algorithm, that is, the Goddard Profiling Algorithm (GPROF), relative to version-5 PR 2A25 rain rates. These differences, which are expected to diminish for version 6 of the algorithms mainly because of more complex modeling of melting processes and other modifications in GPROF, are within the uncertainties of each algorithm. Additional work needs to be carried out to accurately determine where, in the current range of rain estimates from the various algorithms, the optimal TRMM rain estimates are situated. The NPCA, being an effective generalization of various individual algorithms, can significantly contribute to such an effort.

## 5. Conclusions

A method for estimating precipitation profiles from multifrequency, multiresolution active and passive microwave observations is formulated and examined in this paper. The method is based on physical models that simulate, starting from active observations and a pa-

rameter describing the drop size distribution, the passive observations. The drop size distribution parameter is optimally determined such that an agreement between simulated and observed normalized polarization differences is achieved. The method is applied to 3 months of TRMM TMI and PR data in the domain and observing period of the KWAJEX field campaign.

Results show that estimates consistent with both TMI and PR observations can be obtained with the method. For the area and the period investigated, the mean precipitation amounts and rain rates are 30% greater than those derived from the TRMM 2A25 algorithm. Based upon the KWAJEX data, normalized polarizations calculated from 2A25 are low relative to the observed values, but normalized polarizations calculated using NPCA are less biased. This evidence, together with the fact that the relationships between normalized polarizations and precipitation are quite simple for low frequencies, and are significantly more sensitive to the total extinction in the atmospheric column sampled by the radiometer than to the vertical distribution of precipitation in that column, suggest that NPCA rain estimates are likely to be more accurate than 2A25 estimates. The differences between the NPCA and the TRMM facility combined algorithm's (2B31) rain estimates are more difficult to interpret, given that simplified radiometer–precipitation relationships are used in 2B31, and the residuals between the 2B31 brightness temperature calculations and actual observations are not stored in the final products. A sensitivity analysis reveals some dependency of the NPCA retrievals on the choice of covariance matrices. However, this dependence is smaller than that of PR-only retrievals, which justifies the use of NPCA retrievals even if uncertainties in the covariance matrices are suspected.

The comparison of NPCA estimates with ground radar–based estimates reveals generally good agreement, that is, fairly high correlation and a mean relative difference of about 10%, although some discrepancy in the distributions of rain rates is noted. It appears that the NPCA does not possess sufficient sensitivity to estimate the low-intensity precipitation and consistently overestimates it. The same behavior is noted in the 2A25 and 2B31 algorithms. However, although the NPCA might compensate for undetected precipitation by artificially increasing detected precipitation and may underestimate high-intensity precipitation because of overestimation of nearby low-intensity precipitation, overall estimates are less likely to be biased than estimates from single-instrument algorithms.

Future work must be done to analyze the NPCA's behavior in different regions and seasons. Because the DSDs may very regionally and seasonally, different relationships between the PR and TMI observations are expected. Such an analysis would facilitate the elucidation of the differences between the retrievals from TMI-only (2A12) and PR-only (2A25) algorithms and would provide knowledge for the enhancement of these algorithms. For example, given a certain region and season, agreement between the NPCA and 2A25 and disagreement between the NPCA and 2A12 would indicate an appropriate choice of the *Z–R* relationships used in 2A25 but a deficiency in the cloud model database used in 2A12, while disagreement between the 2A25 and the NPCA would indicate a suboptimal choice of the 2A25 *Z–R* relationships. The remediation of such possible deficiencies would lead to more consistent precipitation estimates from the individual TRMM instruments.

*Acknowledgments.* The authors acknowledge and appreciate useful discussions with Drs. Robert Meneghini and Lin Tian of NASA GSFC. The study was supported by the NASA TRMM Project.

## REFERENCES

Anagnostou, E. N., and W. F. Krajewski, 1999: Real-time radar rainfall estimation. Part I: Algorithm formulation. *J. Atmos. Oceanic Technol.,* **16,** 198–205.

Bauer, P., L. Schanz, and L. Roberti, 1998: Correction of three-dimensional effects for passive microwave remote sensing of convective clouds. *J. Appl. Meteor.,* **37,** 1619–1643.

Bringi, V. N., V. Chandrasekar, J. Hubbert, E. Gorgucci, W. L. Randeu, and M. Schoenhuber, 2003: Raindrop size distribution in different climatic regimes from disdrometer and dual-polarized radar analysis. *J. Atmos. Sci.,* **60,** 354–365.

Ferreira, F., P. Amayenc, S. Oury, and J. Testud, 2001: Study and tests of improved rain estimates from the TRMM precipitation radar. *J. Appl. Meteor.,* **40,** 1878–1899.

Giering, R., and T. Kaminski, 1998: Recipes for adjoint code construction. *ACM Trans. Math. Software,* **24,** 437–474.

Grecu, M., and E. N. Anagnostou, 2002: Use of passive microwave observations in a radar rainfall-profiling algorithm. *J. Appl. Meteor.,* **41,** 702–715.

Haddad, Z. S., E. A. Smith, C. Kummerow, T. Iguchi, M. R. Farrar, S. L. Durden, M. Alves, and W. S. Olson, 1997: The TRMM 'day-1' radar/radiometer combined rain-profiling algorithm. *J. Meteor. Soc. Japan,* **75,** 799–808.

Hinton, B. B., W. S. Olson, D. W. Martin, and B. Auvine, 1992: A passive microwave algorithm for tropical oceanic rainfall. *J. Appl. Meteor.,* **31,** 1379–1395.

Hu, Z., and R. C. Srivastava, 1995: Evolution of raindrop size distribution by coalescence, breakup, and evaporation: Theory and observations. *J. Atmos. Sci.,* **52,** 1761–1783.

Iguchi, T., T. Kozu, R. Meneghini, J. Awaka, and K. Okamoto, 2000: Rain-profiling algorithm for the TRMM precipitation radar. *J. Appl. Meteor.,* **39,** 2038–2052.

Khain, A., M. Ovtchinnikov, M. Pinsky, A. Pokrovsky, and H. Krugliak, 2000: Notes on the state-of-the-art numerical modeling of cloud microphysics. *Atmos. Res.,* **55,** 159–224.

Kozu, T., and T. Iguchi, 1999: Nonuniform beamfilling correction for spaceborne radar rainfall measurement: Implications from TOGA COARE radar data analysis. *J. Atmos. Oceanic Technol.,* **16,** 1722–1735.

Kummerow, C., and Coauthors, 2001: The evolution of the Goddard Profiling Algorithm (GPROF) for rainfall estimation from passive microwave sensors. *J. Appl. Meteor.,* **40,** 1801–1820.

Li, X., and R. C. Srivastava, 2001: An analytical solution for raindrop evaporation and its application to radar rainfall measurements. *J. Appl. Meteor.,* **40,** 1607–1616.

Liao, L., R. Meneghini, and T. Iguchi, 2001: Comparisons of rain rate and reflectivity factor derived from the TRMM precipitation radar and the WSR-88D over the Melbourne, Florida, site. *J. Atmos. Oceanic Technol.,* **18,** 1959–1974.

Magono, C., and T. Nakamura, 1965: Aerodynamic studies of falling snowflakes. *J. Meteor. Soc. Japan,* **43,** 139–147.

Marzano, F. S., A. Mugnai, G. Panegrossi, N. Pierdicca, E. A. Smith, and J. Turk, 1999: Bayesian estimation of precipitating cloud parameters from combined measurements of spaceborne microwave radiometer and radar. *IEEE Trans. Geosci. Remote Sens.,* **37,** 596–613.

Meneghini, R., H. Kumagai, J. R. Wang, T. Iguchi, and T. Kozu, 1997: Microphysical retrievals over stratiform rain using measurements from an airborne dual-wavelength radar-radiometer. *IEEE Trans. Geosci. Remote Sens.,* **35,** 487–506.

——, T. Iguchi, T. Kozu, L. Liao, K. Okamoto, J. A. Jones, and J. Kwiatkowski, 2000: Use of the surface reference technique for path attenuation estimates from the TRMM radar. *J. Appl. Meteor.,* **39,** 2053–2070.

Olson, W. S., C. Kummerow, G. M. Heymsfield, I. J. Caylor, and L. Giglio, 1996: A method of combined passive/active microwave retrievals of cloud and precipitation profiles. *J. Appl. Meteor.,* **35,** 1763–1789.

——, P. Bauer, N. F. Viltard, D. E. Johnson, W.-K. Tao, R. Meneghini, and L. Liao, 2001: A melting-layer model for passive/active microwave remote sensing applications. Part I: Model formulation and comparison with observations. *J. Appl. Meteor.,* **40,** 1145–1163.

Passarelli, R. E., and R. C. Srivastava, 1979: A new aspect of snowflake aggregation theory. *J. Atmos. Sci.,* **36,** 484–493.

Perica, S., and E. Foufoula-Georgiou, 1996: Model for multiscale disaggregation of spatial rainfall based on coupling meteorological and scaling descriptions. *J. Geophys. Res.,* **101,** 26 347–26 361.

Petty, G. W., 1994: Physical retrievals of over-ocean rain rate from multichannel microwave imagery. 2. Theoretical characteristics of normalized polarization and scattering indices. *Meteor. Atmos. Phys.,* **54,** 79–99.

Schols, J. L., and J. A. Weinman, 1994: Retrieval of hydrometeor distributions over the ocean from airborne single-frequency radar and multi-frequency radiometric measurements. *Atmos. Res.,* **34,** 329–346.

Skofronick-Jackson, G. M., J. R. Wang, G. M. Heymsfield, R. Hood, W. Manning, R. Meneghini, and J. A. Weinman, 2003: Combined radiometer–radar microphysical profile estimations with emphasis on high-frequency brightness temperature observations. *J. Appl. Meteor.,* **42,** 476–487.

Smith, E. A., F. J. Turk, M. R. Farrar, A. Mugnai, and X. W. Xiang, 1997: Estimating 13.8-GHz path-integrated attenuation from 10.7-GHz brightness temperatures for the TRMM combined PR-TMI precipitation algorithm. *J. Appl. Meteor.,* **36,** 365–388.

Stewart, R. E., J. D. Marwitz, J. C. Pace, and R. E. Carbone, 1984: Characteristics through the melting layer of stratiform clouds. *J. Atmos. Sci.,* **41,** 3227–3237.

Tao, W.-K., and J. Simpson, 1993: Goddard Cumulus Ensemble model. Part I: Model description. *Terr. Atmos. Oceanic Sci.,* **4,** 35–72.

Testud, J., S. Oury, R. A. Black, P. Amayenc, and X. Dou, 2001: The concept of ''normalized'' distribution to describe raindrop spectra: A tool for cloud physics and cloud remote sensing. *J. Appl. Meteor.,* **40,** 1118–1140.

Weinman, J. A., R. Meneghini, and K. Nakamura, 1990: Retrieval of precipitation profiles from airborne radar and passive radiometer measurements: Comparison with dual-frequency radar measurements. *J. Appl. Meteor.,* **29,** 981–993.